SIMULATIONS OF MAGNETIC RECONNECTION FROM CENTRIFUGAL BREAKOUT

by

Christopher M. Bard

A thesis submitted to the Faculty of the University of Delaware in partial fulfillment of the requirements for the degree of Honors Bachelor of Science with Distinction in Physics

May 2010

SIMULATIONS OF MAGNETIC RECONNECTION FROM CENTRIFUGAL BREAKOUT

by

Christopher M. Bard

Approved: ____

Michael Shay, Ph.D.
Professor in charge of thesis on behalf of the Advisory Committee

Approved: ____

Stanley Owocki, Ph.D.
Committee member from the Department of Physics

Approved: ____

Pak-Wing Fok, Ph.D.
Committee member from the Board of Senior Thesis Readers

Approved: ____

Alan Fox, Ph.D.
Director, University Honors Program

TABLE OF CONTENTS

LIST OF FIGURES

LIST OF TABLES

ABSTRACT

This thesis is the first step toward the goal of modeling centrifugal breakout from massive stars while including realistic magnetic reconnection physics. We use a plasma-physics based approach to analyze the magnetic reconnection which occurs in a stellar magnetosphere during centrifugal breakout. We modify a magentohydrodynamic code and test it by simulating an Alfvén wave and a Rayleigh-Taylor instabilities. The properties of the wave and the growth rate of the instability are derived in order to confirm the code's accuracy in the benchmarking. After this, a simple model of centrifugal breakout is developed which incorporates centrifugal force, gravity, and magnetic tension. Local density sources which imitate the accumulation of mass during centrifugal breakout are found to be a viable cause of magnetic reconnection.

Chapter 1

INTRODUCTION

In space plasmas, there are many examples of magnetic phenomena, such as solar flares, coronal mass ejections, and Earth's aurora. These events are believed to be powered by the release of magnetic energy through a process called "magnetic reconnection". One particular event that could be driven by reconnection is X-ray flares. In flares on the Sun, regions with very large magnetic fields suddenly emit very strong X-rays for minutes at a time and plasma can be seen blasting away from the Sun. There have also been X-ray flares observed in stars such as σ Ori E [5], which is a very hot star that lacks the convection zone thought to drive the magnetic activity of cooler stars like the Sun. However, σ Ori E has an observed dipole magnetic field that is very strong and large. Because of this, it is unclear how its magnetic field lines can develop the small scales needed to undergo reconnection. One possible cause of the X-ray flares in σ Ori E or other massive magnetic stars is centrifugal breakout. A better understanding of magnetic reconnection in the context of centrifugal breakout would help us better understand the physical processes that lead to observed X-ray flares. Previous work in centrifugal breakout has been done by ud-Doula and Owocki [2], but the code used to model the breakout was based on an ideal magnetohydrodynamic (MHD) formalism that ignored some complex behavior of plasmas, including processes that could heat material through the dissipation of energy. Magnetic reconnection in their code was actually enabled by a numerical effect caused by the finite spatial grid resolution. The ultimate goal of this work is to model centrifugal breakout from massive stars while including realistic magnetic reconnection physics. In this thesis, we take the first steps toward that goal, benchmarking a basic MHD code with waves and basic interchange instabilities similar to centrifugal breakout, and finally simulating breakout reconnection caused by local density sources.

1.1 Basic Magnetohydrodynamics

Ideally, a large-scale simulation with a very small grid scale incorporating the star, its magnetic field, and the outflow of mass off the stellar surface would be used to study centrifugal breakout. However, including realistic reconnection physics in such a code is too expensive in terms of computational power and time. Thus, one goal in this study is to examine centrifugal breakout in a small, simple system that is able to capture key elements while still incorporating enough plasma physics to allow an accurate representation of reconnection. In order to better understand large-scale plasmas like those found in stars, we use a Magnetohydrodynamic (MHD) model, a combination of fluid mechanics and electromagnetism.

1.1.1 Key Assumptions of MHD

The MHD model involves a few assumptions and simplifications in order to make large-scale simulations possible. One of these assumptions is that the plasma acts as a single fluid. Although the plasma is comprised of individual electrons and positively-charged ions, they are strongly coupled so that the plasma acts as a electrically neutral fluid. Additionally, we assume that the model is being applied on length scales much larger than the collisional mean free path, which is the average distance a particle travels in the plasma before colliding into another particle. We also assume the simulation length scales are much larger than other plasma length scales like the Debye length and the Larmor radius. The Debye length is the scale over which the charge of an ion within the plasma is canceled out locally by nearby electrons, while the Larmor radius is the radius of the circular motion of a charged particle in the presence of a magnetic field. During conditions found in stellar atmospheres, these length scales are on the order of a few meters. This is much smaller than the model length scales defined by stellar radii of millions of kilometers. We also apply the model on time scales much larger than the mean collision time, the time it takes for a particle to collide with another particle. These assumptions of large spatial and time lengths allows us to treat the plasma as a single fluid, since we do not have to model each specific interaction between the particles. Finally, in the plasma, the free electrons are able to very effectively carry electric current, resulting in a very high conductivity. In a particular MHD model known as "ideal MHD", the conductivity of the plasma is assumed to be infinite.

1.1.2 Magnetic Induction vs. Diffusion

Since plasmas are comprised of electrons and positively-charged ions, their behavior is affected by electric and magnetic fields. The set of equations representing the change of an electric field **E** and a magnetic field **B** are known as Maxwell's equations:

$$\nabla \cdot \mathbf{E} = 4\pi\rho_c \tag{1.1}$$

$$\nabla \times \mathbf{E} = -\frac{1}{c}\frac{\partial \mathbf{B}}{\partial t} \tag{1.2}$$

$$\nabla \cdot \mathbf{B} = 0 \tag{1.3}$$

$$\nabla \times \mathbf{B} = \frac{4\pi}{c}\mathbf{J} + \frac{1}{c}\frac{\partial \mathbf{E}}{\partial t} \tag{1.4}$$

In basic MHD, we assume that there is no net macroscopic charge density, so $\rho_c = 0$. We also assume that the Maxwell displacement current is negligible ($\frac{\partial \mathbf{E}}{\partial t} \to 0$), giving $\mathbf{J} = \frac{c}{4\pi}\nabla \times \mathbf{B}$, where $\mathbf{J}$ is the current density. The electric field is modeled in terms of a general Ohm's law:

$$\mathbf{E} = \frac{-v}{c} \times \mathbf{B} + \frac{1}{\sigma}\mathbf{J} \ , \tag{1.5}$$

where σ is the conductivity of the plasma and v is the flow velocity of the plasma. If we apply eq. (1.5) to (1.4) and take the curl of the resultant equation to apply in (1.2), after using some vector identities, we get the equation

$$\frac{\partial \mathbf{B}}{\partial t} = \nabla \times (v \times \mathbf{B}) + \frac{c^2}{4\sigma} \nabla^2 \mathbf{B} \tag{1.6}$$

The first term of the right hand side represents the effect of magnetic induction while the second term represents the effect of magnetic diffusion. The ratio between the two effects can be described with the magnetic Reynolds number:

$$R_m \approx \frac{4\pi\sigma L v}{c^2} \ , \tag{1.7}$$

where L represents the characteristic length scale for the gradient in the magnetic field. In the stellar atmosphere, this length scale is on the order of the stellar radius. A characteristic value for v in the stellar atmosphere can range from the sound speed, 20 km/s, to the stellar escape speed, 600 km/s. Partially due to the high plasma conductivity $\sigma \approx 10^{10}\,\mathrm{s}^{-1}$, the magnetic Reynolds number is usually of order $R_m \approx 10^{10}$. This means that the effect of diffusion on the magnetic field can be ignored in these situations. This is especially true in ideal MHD, where the plasma is assumed to have an effectively infinite conductivity.

1.1.3 Frozen-In Magnetic Field Lines

In ideal MHD, the assumption of infinite conductivity in the plasma leads to a condition known as "frozen-in" magnetic field lines. If the conductivity is taken to be infinite, the magnetic Reynolds number (1.7) is also infinite. This means that the effects of diffusion can be ignored, so (1.6) can be simplified to:

$$\frac{\partial \mathbf{B}}{\partial t} = \nabla \times (v \times \mathbf{B}) \tag{1.8}$$

Using equations (1.3), (1.8), and the divergence and Stokes' theorems from vector calculus, we can show that the net magnetic flux through any surface S, $\Phi = \int_S \mathbf{B} \cdot$

$d\mathbf{A}$, does not change with time, i.e. $d\Phi/dt = 0$. This is Alfvén's frozen flux theorem, which states that the motion of the plasma is fastened to the magnetic field lines and that the magnetic flux through a surface moving with a perfectly conducting plasma is conserved [7]. A result of this theorem is that each parcel of plasma is confined to its local magnetic field line. It cannot ever move to a different field line. Also, if the energy density of the plasma is greater than the magnetic field, the flow of the plasma can force the magnetic field lines to move. Alternatively, if the magnetic field has a greater energy density, the field lines can stay where they are and channel the plasma flow. One important thing to remember about the frozen flux theorem is that it only holds for very large values of the magnetic Reynolds number, that is, it only works when the magnetic diffusion is negligible compared to the induction.

1.1.4 Magnetic Tension and Pressure

The force of the magnetic field line on the plasma can be quantified by the Lorentz force:

$$F_B = \frac{\mathbf{J} \times \mathbf{B}}{c} = \frac{(\nabla \times \mathbf{B}) \times \mathbf{B}}{4\pi} = \frac{\mathbf{B} \cdot \nabla \mathbf{B}}{4\pi} - \nabla(\frac{\mathbf{B}^2}{8\pi}) \; , \tag{1.9}$$

where the second equality comes from equation (1.4) with the MHD assumption that $\frac{\partial \mathbf{E}}{\partial t} \rightarrow 0$. The third equality uses vector identities to arrive at two separate force terms, the first a result of magnetic tension and the other the result of magnetic pressure. Magnetic tension is a force that acts to straighten curved magnetic field lines, similar to the force that acts to restore a stretched rubber band to its non-stretched state. Due to the frozen-in condition, as the plasma moves, the magnetic field lines move with the plasma. This can result in the bending of the magnetic field lines; as the curvature of the field lines increases, the magnetic tension increases. The magnetic pressure is similar to air pressure, except the energy is carried by the magnetic field rather than the motion of particles. When many magnetic field lines

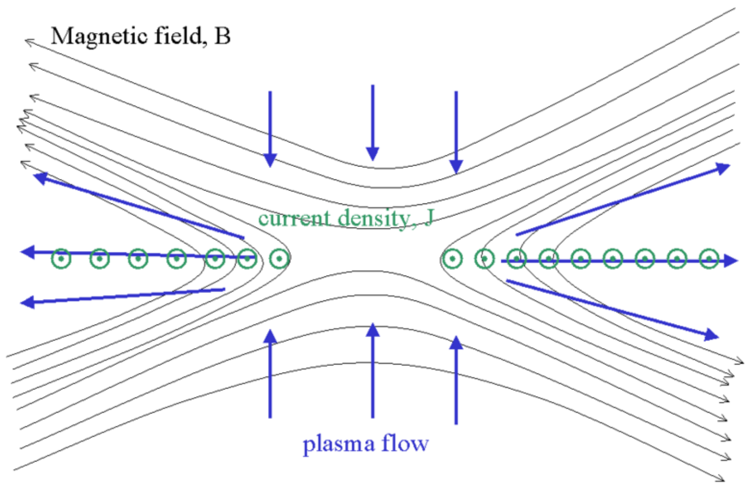

Figure 1.1: The process of magnetic reconnection. The magnetic field lines at the top and bottom of the figure move toward the middle, where they break and reconnect. The reconnected lines move outwards, to the left and right.

are close together, they have more magnetic pressure than a smaller amount of field lines close together. This is analogous to a greater density of air having a higher pressure than a lower density of air. Another important property of the magnetic pressure is that it only acts perpendicular to the magnetic field lines. This causes the magnetic pressure to be anisotropic, in contrast to isotropic pressure in air. In a plasma that has frozen-in magnetic field lines, the magnetic pressure opposes the compression of field lines due to plasma motion.

1.2 Magnetic Reconnection

In plasmas, the frozen flux theorem governs the motions of the plasma and the magnetic field lines. However, in the course of plasma flow, it is possible that two separate regions of plasmas could flow towards each other. As the separate flows come together, the magnetic field lines also come together. This compression of magnetic field lines reduces the length scale for the gradient in the magnetic field,

L (from eq. (1.7)). When the field lines are compressed enough, L becomes so small that the magnetic Reynolds number approaches 1. As a result, diffusion is no longer negligible, and the frozen flux theorem is no longer applicable. This leads to the breaking of the magnetic field lines, which are then arranged into different domains. This is a process known as "magnetic reconnection", illustrated in Figure 1.1. In this simple reconnection, the plasma flows from the top and the bottom compress the magnetic field lines in the center where they break. They reconnect into different domains and flow out the sides. One consequence of reconnection is the mixing of previously distinct regions of plasma. Because the magnetic field lines are "frozen into" the plasma, their topology prevents plasma in different regions from mixing. However, during reconnection, plasma from different areas mix together as the magnetic domains change. Another consequence of reconnection is that the magnetic energy stored in the tension of the field lines is released when they break. This influx of energy into the plasma heats it up. As the plasma cools, it gives off energy, such as X-ray flares, that we can observe.

1.3 Centrifugal Breakout

Reconnection occurs when the frozen-in field lines are compressed to such small length scales that the effect of magnetic diffusion can no longer be ignored. However, in stars such as σ Ori E, the magnetic field is so strong that the magnetic field lines are rigid and highly resistant to compression that would result in reconnection. However, we know that reconnection is occurring in σ Ori E, since we have observed X-ray flares emanating from the star [5]. So what causes the field lines to reconnect? One theory states that centrifugal breakout is the mechanism which drives reconnection in these highly magnetic stars, like σ Ori E.

1.3.1 Magnetic Confinement Parameter

In order to discuss centrifugal breakout, we must first understand some important concepts. One of these is the wind magnetic confinement parameter, η_*, as defined by ud-Doula and Owocki [4]. This dimensionless parameter describes the result of the interaction between the stellar wind and magnetic field tension. The stellar wind is comprised of particles flowing away from the surface of the star. In hot stars, like σ Ori E, the radiation pressure of the light is what causes the outflow of plasma from the star. If the stellar magnetic field has a higher energy density than the stellar wind, the plasma will be channeled along the magnetic field lines and be unable to escape into space. On the other hand, if the stellar wind has a higher energy density, the magnetic field lines will be unable to contain the stellar wind. To derive this parameter, we start with the ratio between the energy densities of the stellar magnetic field and the wind outflow:

$$\eta \equiv \frac{B^2/8\pi}{\rho v^2/2} \ , \tag{1.10}$$

where B_* and R_* are the surface magnetic field and radius of the star, respectively. For convenience, we can rewrite the wind energy density in terms of a spherically symmetric wind-loss rate $\dot{M} = 4\pi r^2 \rho v$:

$$\eta \approx \frac{B^2 r^2}{\dot{M} v} \tag{1.11}$$

Finally, we wish to characterize the radial variation of outflow velocity in terms of a velocity law. Using the terminal wind velocity v_∞, the velocity is given by $v(r) = v_\infty(1 - R_*/r)$. Additionally, we wish to model the magnetic field as a dipole. This results in $B(r) = B_*(R_*/r)^q$, where $q = 3$ for a dipole. Putting these terms for the velocity and magnetic field in 1.11 yields:

$$\eta(r) = \frac{B_*^2 R_*^2}{\dot{M} v_\infty} \frac{(r/R_*)^{2-2q}}{1 - R_*/r} \tag{1.12}$$

In looking at (1.12), we notice that the spatial variations are confined to the right fraction. As a result, the left fraction is a dimensionless parameter that characterizes the relative strength of the magnetic field versus the wind outflow. Thus we have a wind magnetic confinement parameter

$$\eta_* \equiv \frac{B_*^2 R_*^2}{\dot{M} v_\infty} \ . \tag{1.13}$$

From η_*, we see that magnetic confinement of stellar wind depends on both the magnetic field strength and the mass-loss rate of stars.

1.3.2 Alfvén and Keplerian Radii

Other important parameters to consider are the Alfvén radius and the Keplerian radius. The Alfvén radius, R_A is the distance at which the energy densities of the magnetic field and the stellar wind are equal. Another way to consider the Alfvén radius is that it represents the maximum radius of a closed magnetic field line loop emanating from the surface of the star. A loop with $r > R_A$ will result in the stellar wind overwhelming the magnetic field strength. To quantify the Alfvén radius, we can use the wind magnetic confinement parameter since it is the ratio of magnetic field energy density to stellar wind energy density. For simplicity, we ignore the wind velocity variation, taking $v(r) = v_\infty$. Setting (1.13) to equal one and solving for the radius yields the Alfvén radius:

$$R_A = \eta_*^{1/4} R_*. \tag{1.14}$$

For $r < R_A$, we expect the magnetic field to dominate the stellar wind and prevent the plasma from flowing into space. The star's gravity will then pull the plasma back towards the surface. However, as part of the centrifugal breakout model, we assume that the plasma is confined in a rigidly rotating magnetosphere (RRM), which will be discussed in a later section. Essentially, the RRM causes the plasma to rotate at the same angular speed as the star, so the rotational velocity of the plasma is given by $v = \Omega r$, where Ω is the angular velocity of the star and r is the plasma's distance from the star. This results in a centrifugal force away from the star on the plasma.

Thus, there are three major forces on the plasma: gravity, centrifugal force, and the magnetic field tension. For $r < R_A$, the magnetic field tension dominates the other forces and prevents the plasma from escaping. However, due to the centrifugal force, not all plasma confined by the magnetic field will fall back to the star. There is a point a certain distance away from the star before which plasma will fall back to the star and after which the centrifugal force will push the plasma away from the star. We can thus define this as the Keplerian radius, the distance at which the centrifugal force on the plasma balances out the gravitational force from the star. Quantifying this equlibrium, we have

$$\frac{v^2}{R_K} = \frac{GM_*}{R_K^2} \ , \tag{1.15}$$

where G is the gravitational constant, M_* is the mass of the star, and v is the rotational speed of the plamsa. Using the rotational period P, we can write the velocity at the Keplerian radius as $v = 2\pi R_K/P$, where the left part of the fraction represents the distance traveled by the plasma in one rotational period. Substituting this for v in (1.15) and solving for the Keplerian radius yields:

$$R_K = \sqrt[3]{\frac{GM_*P^2}{(2\pi)^2}} \tag{1.16}$$

1.3.3 Rigidly Rotating Magnetosphere Model

Townsend and Owocki (2005) developed a Rigidly Rotating Magnetosphere (RRM) model to explain hydrogen emission in hot stars with strong magnetic fields [3]. In these stars, the large magnetic field leads to a large magnetic confinement ($\eta_* >> 1$). Since the magnetic confinement is so large, the field lines out from the star are essentially rigid, i.e. they are fixed in place with respect to the stellar surface. This means that any outflow of plasma from the stellar surface will be confined by the field lines. Because of this confinement, the orbital speed of the plasma is directly related to the rotation rate of the star, i.e. $v_\phi = \Omega r$, where Ω

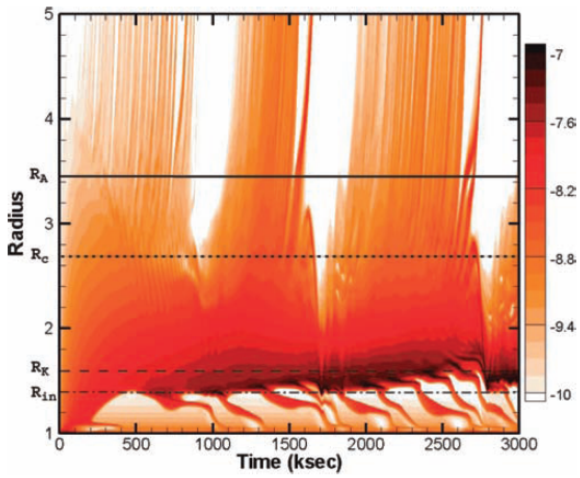

Figure 1.2: A simulated rigidly rotating magnetosphere [8]. The logarithm of the radial distribution of mass is plotted versus time and radius (in units of stellar radius). The darker areas indicate a higher concentration of mass. The Alfvén radius (R_A) is indicated by the solid line and the Keplerian radius (R_K) is indicated by the dashed line. Note the high concentration of mass near the Keplerian radius.

is the rotation rate of the star. Consequently, the centrifugal force is greater at a larger distance from the star. Any plasma confined along the magnetic field lines at a distance $r < R_k$ will fall back to the surface due to the gravitational force overwhelming the centrifugal force. However, any plasma outside the Keplerian radius will not fall back, since the increased centrifugal force farther away from the star balances or exceeds the gravitational force pulling the plasma back towards the star. However, as long as the magnetic confinement remains large, $R_A > R_k$. In the region $R_k < r < R_A$, the tension in the field lines will balance the net gravitational-centrifugal force on the plasma. The plasma then stays at equilibrium, but will continue to accumulate due to the stellar wind. This results in a magnetosphere rotating rigidly with the star at radius r, where $R_K < r < R_A$. An illustration of a RRM is shown in Figure 1.2. There is a very high concentration of mass near the Keplerian radius, since that is where the centrifugal and gravitational forces on the

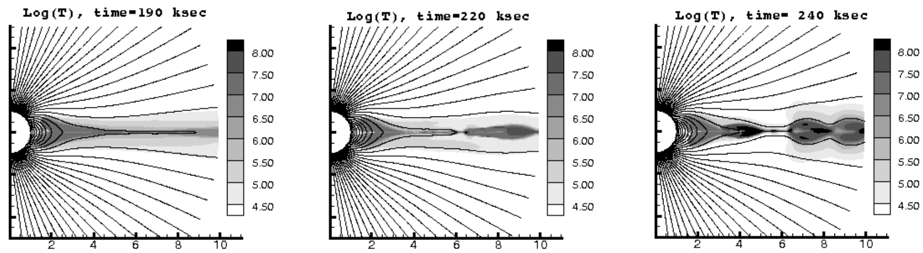

Figure 1.3: The progression of centrifugal breakout[2]. The leftmost picture shows the stretching of the magnetic field line into a thin loop, causing reconnection (middle). The heating caused by the breakout of stellar mass occurs on the right.

plasma are at equilibrium. Between R_K and R_A, the tension in the magnetic field lines acts to balance out the net gravitational-centrifugal force. This confines the plasma in a rigidly rotating magnetosphere.

1.3.4 Centrifugal Breakout

The plasma within a star's RRM is at equilibrium, but plasma will continue to flow off the surface and accumulate in the magnetosphere over time. Since centrifugal force is directly proportional to mass, this accumulation of plasma will cause an increase in the centrifugal force. However, the magnetic field declines as a factor of $1/r^3$ (eq. 1.12) and its energy density declines as a factor of $1/r^6$. This decline of the magnetic field strength coupled with the increase of centrifugal force allows the plasma's energy density to overwhelm the magnetic field energy density. As a result, the mass of plasma moves away from the star and drags the frozen-in field lines with them. This results in a stretching of the field lines since the magnetic tension opposes this outward movement, much like the tension in a rubber band opposes the force stretching it out. When the plasma moves far enough out, the field lines are forced close enough together to start the reconnection process. They break and reconnect, resulting in a breakout of mass. This process is shown in Figure 1.3. The energy released during reconnection results in the heating of the

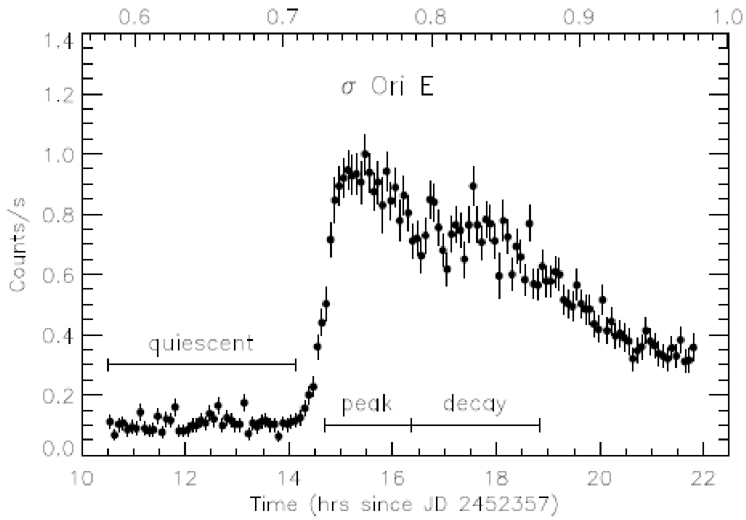

Figure 1.4: The X-ray light curve of σ Ori E, as measured by Sanz-Forcada et al. [5] The peak in the graph is an X-ray flare, which is possibly caused by centrifugal breakout as theorized by ud-Doula and Owocki [2]

plasma. It is theorized that this heating of the plasma results in the emission of X-ray flares [2], like those seen in the star σ Ori E (Figure 1.4).

We can estimate the characteristic time scale for centrifugal breakout, i.e. how often breakout occurs. First, we consider the breakout condition in the simple case of an aligned dipole field. The breakout condition occurs when the magnetic tension in the field lines is roughly equal to the combined gravitational and centrifugal forces. Expressed quantitatively, the condition is:

$$\rho_b(\Omega^2 r - \frac{GM_*}{r^2}) \approx \frac{B^2}{4\pi h_m}, \tag{1.17}$$

where ρ_b represents a breakout value for the peak density at at radius r within the equatorial plane and h_m is the curvature radius of the tensed magnetic field lines. The left term in the parentheses represents the centrifugal force while the right term represents the gravitational force. The right hand side of the equation is the force arising from magnetic tension. When the density in the RRM reaches ρ_b, breakout occurs. Townsend and Owocki [3] defined a characteristic breakout

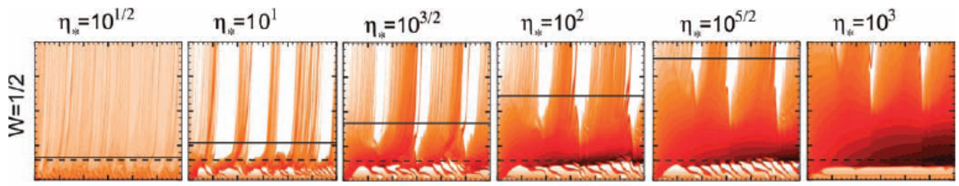

Figure 1.5: Plots of the logarithm of the radial distribution of mass versus time and radius (in units of stellar radius). The darker areas indicate a higher concentration of mass. W represents the rotational speed of the star, and η_* represents the magnetic confinement parameter. For higher values of eta_*, there are less occurrences of centrifugal breakout, represented by the white spaces.

time $t_b = \sigma_b/\dot{\sigma}_m$, where σ_b is the characteristic surface density of plasma in the magnetosphere required for breakout and $\dot{\sigma}_m$ is the surface density accumulation rate:

$$\sigma_b = \frac{B_*^2 \xi_*^4}{4\pi g_*} \frac{\sqrt{\pi}}{\xi^4(\xi^3 - 1)} \tag{1.18}$$

$$\dot{\sigma}_m = \mu_* \frac{\eta_*^3}{\eta^3} \frac{\dot{M}}{2\pi R_*^2}, \tag{1.19}$$

where $\xi = R/R_k$ is a scaling of the local radius, $\xi_* = R_*/R_k$ is a scaling of the stellar radius, and μ_* is the molecular weight of the stellar material. Noting that stellar gravity can be expressed in terms of the surface escape speed and free-fall time, $g_* = v_{esc}/2t_{ff}$, we can express the ratio of breakout to free-fall time as:

$$\frac{t_b}{t_{ff}} = \eta_* \frac{\pi}{\mu_*} \frac{\xi_*}{\xi(\xi^3 - 1)} \tag{1.20}$$

We thus see that breakout time is dependent on the magnetic confinement parameter η_* (eq. 1.13) and the distance from the star (ξ). When the magnetic field is stronger, breakout occurs less frequently. This principle is illustrated in Figure 1.5. The white areas of the plots represent regions of centrifugal breakout. The plasma, after breaking out, has vacated these regions, leading to a lower density. As the magnetic confinement increases, these regions become less frequent, indicating that the breakout time is higher. For plasma farther away from the star, breakout occurs more frequently than for plasma closer to the star. This is illustrated in Fig. 1.2. The breakout regions that begin closer to the star happen less frequently than the regions that begin farther away from the star, indicating that breakout time is larger for distances closer to the star. Using values corresponding to σ Ori E for the parameters in (1.20), we can simplify the breakout time equation as a function of scale distance from the star ξ:

$$t_b(\xi) \approx 250\,\mathrm{yr}\,\frac{12.5}{\xi(\xi^3 - 1)}\ . \tag{1.21}$$

Using this equation, the breakout time for the plasma a distance of $2R_K$ ($\xi = 2$) from the star is estimated to be about 220 years. This indicates that the full breakout of material is a relatively frequent occurrence over the billions-of-years lifetime of a star, but rare during a human lifetime. However, for plasma on the outer edge of the RRM farther away from the star ($\xi \approx 13$), the breakout time can be as small as a few weeks. This indicates that small-scale breakouts are much more common; these breakouts could be the cause of the X-ray flares we observe on stars like σ Ori E.

Chapter 2

THE SIMULATION CODE

The simulation code was based on a program written by Adil Hassam [1] and modified to incorporate our model.

2.1 Magnetohydrodynamic Equations

The model uses the magnetohydrodynamic (MHD) equations in order to incorporate the physics of plasmas within it. The equations consist of a density equation, a force equation, and a magnetic field equation, where n represents the density, g is the acceleration due to gravity, p is the pressure, J_p is the mass flow and u is the flow velocity, with $J_p = nu$. The equations are then normalized so that all variables become dimensionless. This creates a generalized simulation that can represent many actual physical situations, including centrifugal breakout. These equations are:

$$\frac{\partial \vec{\bar{n}}}{\partial \bar{t}} + \vec{\bar{\nabla}} \cdot \vec{\bar{J}}_p = 0 \tag{2.1}$$

$$\frac{\partial \bar{J}_p}{\partial \bar{t}} + \vec{\bar{\nabla}} \cdot (\vec{\bar{u}}\vec{\bar{J}}_p) = \vec{\bar{J}} \times \vec{\bar{B}} - \vec{\bar{\nabla}}\bar{p} - \bar{n}\bar{g}\hat{x} \tag{2.2}$$

$$\frac{\partial \vec{\bar{B}}}{\partial \bar{t}} = \vec{\bar{\nabla}} \times \vec{\bar{u}} \times \vec{\bar{B}}, \tag{2.3}$$

Throughout the rest of this paper, all equations are normalized, though the variables appear without a bar. The model is two-dimensional in the $\hat{x}$ and $\hat{z}$ directions with $\hat{y}$ out of the page. We separate the magnetic field into planar ($\hat{x}$ and $\hat{z}$) and transverse ($\hat{y}$) components. The magnetic field in the plane of the box is represented by the equation $\hat{y} \times \vec{\nabla}\psi$, where ψ is a scalar field. The transverse magnetic field is represented by: $\vec{B_y} = B_{y0}\ \hat{y}$. The equations (2.1), (2.2), and (2.3) are simplified using the conventions for the magnetic field and then rearranged to obtain the time derivatives of all variables in terms of their spatial derivatives. In addition, the pressure is written as $p = nT$, where T is the temperature. The final equations are:

$$\frac{\partial n}{\partial t} = -\frac{\partial J_{px}}{\partial x} - \frac{\partial J_{pz}}{\partial z} \tag{2.4}$$

$$\frac{\partial \psi}{\partial t} = -(u_x \frac{\partial \psi}{\partial x} + u_z \frac{\partial \psi}{\partial z}) \tag{2.5}$$

$$\frac{\partial B_y}{\partial t} = (\frac{\partial u_y}{\partial x}\frac{\partial \psi}{\partial z} - \frac{\partial u_y}{\partial z}\frac{\partial \psi}{\partial x}) - \frac{\partial}{\partial x}(u_x B_y) - \frac{\partial}{\partial z}(u_z B_y) \tag{2.6}$$

$$\frac{\partial J_{pz}}{\partial t} = -\frac{\partial}{\partial x}(u_x J_{pz}) - \frac{\partial}{\partial z}(u_z J_{pz}) - \frac{\partial \psi}{\partial z}(\frac{\partial^2 \psi}{\partial x^2} + \frac{\partial^2 \psi}{\partial z^2}) - \frac{\partial}{\partial z}\frac{B_y^2}{2} - \frac{\partial}{\partial z}(nT) \tag{2.7}$$

$$\frac{\partial J_{py}}{\partial t} = -\frac{\partial}{\partial x}(u_x J_{py}) - \frac{\partial}{\partial z}(u_z J_{py}) - (\frac{\partial B_y}{\partial z}\frac{\partial \psi}{\partial x} - \frac{\partial B_y}{\partial x}\frac{\partial \psi}{\partial z}) \tag{2.8}$$

$$\frac{\partial J_{px}}{\partial t} = -\frac{\partial}{\partial x}(u_x J_{px}) - \frac{\partial}{\partial z}(u_z J_{px}) - \frac{\partial \psi}{\partial x}(\frac{\partial^2 \psi}{\partial x^2} + \frac{\partial^2 \psi}{\partial z^2}) - \frac{\partial}{\partial x}\frac{B_y^2}{2} - \frac{\partial}{\partial x}(nT) - ng \tag{2.9}$$

Another MHD equation in addition to the ones above is the adiabatic equation of state for an ideal gas:

$$\frac{\partial}{\partial t}(\frac{p}{n^\gamma}) = 0\ , \tag{2.10}$$

where $\gamma = 5/3$. In addition to the MHD equations listed above, we also take into account the diffusion of the plasma. To incorporate the diffusion effect, we use the ability of Fick's second law to predict how the diffusion causes the concentration field to change over time:

$$\frac{\partial \theta}{\partial t} = D\nabla^2\theta\ , \tag{2.11}$$

where θ represents the parameter (n, J_{px}, etc.) and D is the diffusion coefficient. The right side of (2.11) is added to each of the MHD equations to incorporate diffusion.

2.2 Alfvén Wave

One of the benchmarks we used to test the code is an Alfvén wave. An Alfvén wave is a oscillation of the magnetic field lines similar to the vibration of a plucked guitar string. In an Alfvén wave, the magnetic field (B_z) and the mass flow velocity (u_z) should oscillate sinusoidally, both 180° out of phase with respect to each other. The propagation of the Alfvén wave is shown in Figure 2.1. We can derive the Alfvén wave perturbation by linearizing equations (2.1), (2.2), and (2.3) using $n = n_0 + \tilde{n}$, $u = u_0 + \tilde{u}$, and $B = B_0 + \tilde{B}$. To simplify this theoretical derivation, we will ignore the effects of diffusion. For an Alfvén wave, there is no density perturbation, so $\tilde{n} = 0$. There is no initial flow velocity ($u_0 = 0$) and the flow perturbation is only in the $\hat{z}$ direction, so $u = \tilde{u_z}$. There is no transverse magnetic field and the magnetic field perturbation is only in the $\hat{z}$ direction, so $B = B_{x0}\hat{x} + \tilde{B}_z\hat{z}$. Since we use ψ to represent the planar magnetic field, we define $\psi = \psi_0 + \tilde{\psi} = B_{x0}z + \tilde{\psi}$ so that we get our desired B from $B = \hat{y} \times \nabla\psi$. Additionally, there is no gravitational force, so $g = 0$. Finally, we remember $J_p = nu$, so that when linearized, $J_p = n_0\tilde{u}$. Taking all these considerations and applying them to (2.2) and (2.3) yields:

$$n_0 \frac{\partial \tilde{u_z}}{\partial t} = \nabla^2 \tilde{\psi} \ \nabla \psi_0 \tag{2.12}$$

$$\frac{\partial \tilde{\psi}}{\partial t} = \tilde{u_z} \frac{\partial}{\partial z} \psi_0 \tag{2.13}$$

Now, since the perturbations have the form $\tilde{n}(x)e^{i(kz-\omega t)}$, $\tilde{u}(x)e^{i(kz-\omega t)}$, and $\tilde{\psi}(x)e^{i(kz-\omega t)}$ we can Fourier decompose along $\hat{z}$. This has the effect of replacing all $\frac{\partial}{\partial z}$ with ik and all $\frac{\partial}{\partial t}$ with $-i\omega$. Additionally, because we defined $\psi_0 = B_{x0}z$, we can take $\frac{\partial}{\partial z}\psi_0 = B_{x0}$. After Fourier decomposing, we get the equations:

$$i\omega n_0 \tilde{u_z} = -k^2 B_{x0} \tilde{\psi} \tag{2.14}$$

$$-i\omega \tilde{\psi} = \tilde{u_z} B_{x0} \tag{2.15}$$

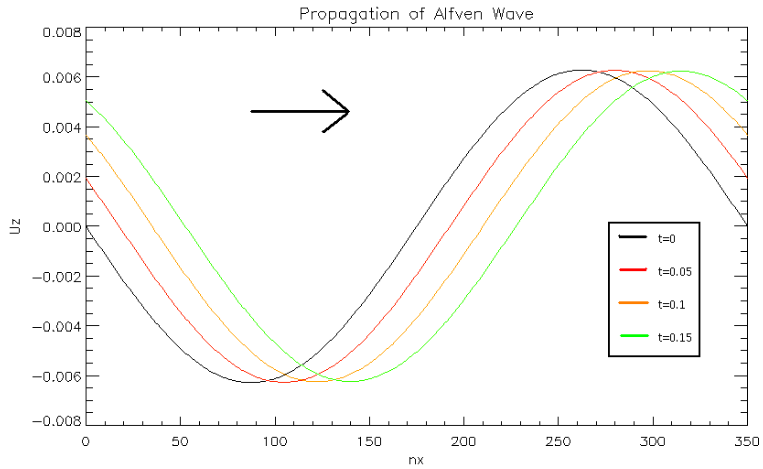

Figure 2.1: The propagation of the Alfvén wave. The arrow indicates the direction of propagation.

Solving (2.15) in terms of $\tilde{\psi}$ and substituting in (2.14) allows us to solve for the dispersion relation, ω:

$$\omega = \frac{kB_{x0}}{\sqrt{n}} \tag{2.16}$$

In order to implement the Alfvén wave in the code, we have to define the variables according to our methodology above. Based on our definition for ψ above, we get $B_x = B_{x0}$ and $B_z = ikB_{z0}e^{ikx}$. The real part of B_z is $kB_{z0}\sin(kx)$. We can use this definition of B_z in (2.15) to get $u_z = -ku_0\sin(kx)$. Thus, we use the initial conditions:

$$\begin{aligned}
u_z &= -ku_0 sin(kx) \\
B_z &= kB_0 sin(kx) \\
k &= 2\pi \\
B_x &= 1 \\
n &= 1
\end{aligned}$$

Since B_x and B_z are obtained from ψ, we define $\psi = z + B_0 cos(kx)$, which gives us the desired B_x and B_z values. The boundary conditions of the simulation are set to

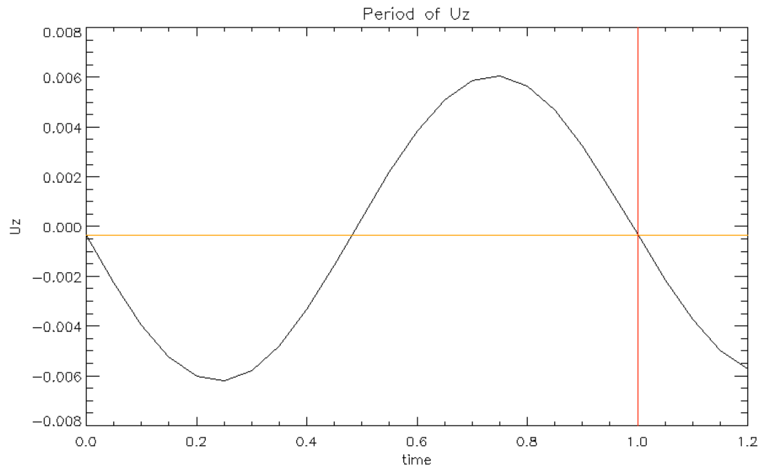

Figure 2.2: The period of the simulated Alfvén wave. The black line is the simulated Alfvén wave. The horizontal orange line represents the initial value of u_z at $t = 0$ and the vertical red line represents $t = 1$. The point at which the orange and red lines intersect is the predicted value for u_z after one period. Since the black line also intersects at this point, the computational period of the wave matches the predicted period.

periodic in both the $\hat{x}$ and $\hat{z}$ directions. This means that if the wave goes out of one side of the box, it will come in the opposite side. In order to check the accuracy of the simulated Alfvén wave, we need to verify that the theoretical ω of the wave is consistent with the experimental ω. The angular frequency of the wave (eq. 2.16) is $\omega = kB_{x0}/\sqrt{n_0} = k = 2\pi$, since B_{x0} and n_0 are both set to 1. The theoretical frequency of the wave is thus $f = \omega/2\pi = 2\pi/2\pi = 1$. This means that the predicted period of the wave is $1/f = 1$ We can check the frequency of our simulated Alfvén wave by plotting the value of u_z at a point in the box against time. This plot is shown in Figure 2.2. Since the value of u_z at $t = 0$ matches the value of u_z at $t = 1$, we see that the theoretical period of the wave matches the computational period of the wave.

In the above derivation of the dispersion function, we ignored the effects of diffusion (eq. 2.11). Because our code implements diffusion, this has the effect of damping the wave over time. As a result, the dispersion relation changes from (2.16)

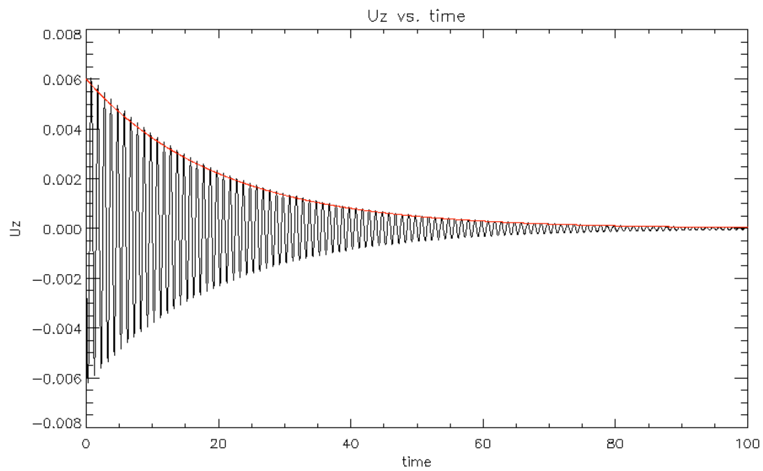

Figure 2.3: The damping of the Alfvén wave. The red line represents the function $0.006e^{-0.05t}$.

to:

$$\omega = kB_{x0}/\sqrt{n_0} + iDk^2 \ , \tag{2.17}$$

where D is a constant indicating the strength of the diffusion. As a result of the added diffusion term, there is an additional damping factor $e^{-i(iDk^2)t} = e^{-\omega_D t}$, where $\omega_D = Dk^2$. As a result, u_z and B_z now have the forms:

$$\begin{aligned} u_z &= -ku_0 sin(kx)e^{-\omega_D t} \\ B_z &= kB_0 sin(kx)e^{-\omega_D t} \end{aligned}$$

Over time, the wave is damped by a factor $e^{-\omega_D t}$. In our simulation, $D = 1.26\times10^{-3}$, so $\omega_D = Dk^2 = 1.26 \times 10^{-3}(2\pi)^2 \approx 0.05$. As a result, the wave should be damped by the factor $e^{-0.05t}$. In order to confirm this, we plot u_z over many periods and fit an exponential function to the peaks of the graph. As shown in Figure 2.3, the exponential function $0.006e^{-0.05t} = 0.006e^{-\omega_D t}$ accurately describes the damping of the Alfvén wave. We see that the predicted damping of the wave matches the computational damping of the wave.

Chapter 3

RAYLEIGH-TAYLOR INSTABLILTY

3.1 Rayleigh-Taylor Equilibrium

A Rayleigh-Taylor equilibrium arises between two fluids with different densities superimposed on top of each other in a gravitational field. Although the bottom fluid has a lower density, it has a higher temperature than the top fluid. This prevents the top fluid from breaking through the interface between the two fluids and causes the system to remain at equilibrium. An illustration of the Rayleigh-Taylor equilibrium is shown in Figure 3.1. Letting P represent the pressure, n the density, and g the gravitational acceleration, we quantify the equilibrium as:

$$\nabla P = \nabla(nT) = -ng \tag{3.1}$$

In order to approximate a constant temperature in the two regions as well as the sharp decrease in temperature across the interface, the functional form of T is set to be:

$$T = 0.5(T_2 - T_1)[\tanh(\frac{x - x_0}{w_0}) + 1] + T_1 \ , \tag{3.2}$$

where x_0 represents the location of the interface within the box and w_0 represents the width of the interface. In order to find the density which satisfies the Rayleigh-Taylor equilibrium, we must solve for density in eq. 3.1, substituing (3.2) for the temperature. Since gravity acts only in the $\hat{x}$ direction, all derivatives of the pressure in the $\hat{y}$ and $\hat{z}$ are equal to zero. This results in the equation:

$$n = \frac{n_0 e^{\frac{-gpx}{T_2 T_1}}}{p + q\tanh(\frac{x-x_0}{w_0})}[q\sinh(\frac{x - x_0}{w_0}) + p\cosh(\frac{x - x_0}{w_0})]^{\frac{w_0 gq}{T_2 T_1}} \ , \tag{3.3}$$

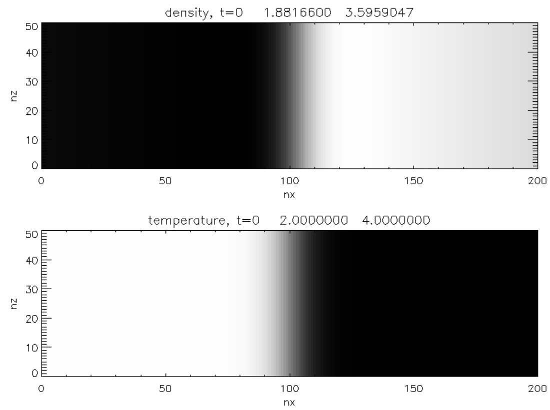

Figure 3.1: 2-D plots of the density and temperature during a Rayleigh-Taylor equilibrium. Gravity acts in the -$\hat{x}$ direction, towards the left of the box. Note that the dark area represents a lower value of the density or temperature.

where $p = 0.5(T_2 + T_1)$ and $q = 0.5(T_2 - T_1)$. Figure 3.2 shows the density and temperature across the simulation box.

3.2 Normal Rayleigh-Taylor Instability

From the MHD code, a model incorporating the Rayleigh-Taylor instability was devised. The instability results from a perturbation in the Rayleigh-Taylor equilibrium causing the upper fluid to break through the interface and cross over into the lower fluid. An example of this instability in action is shown in Figure 3.3. The model was divided into two separate parts: one incorporating a magnetic field perpendicular to the instability and one without an external magnetic field. In order to simplify our theoretical derivation of the growth rate of the instability, we assume that the density and temperature in both regions is constant and that there is a discontinuous jump across the interface between the regions.

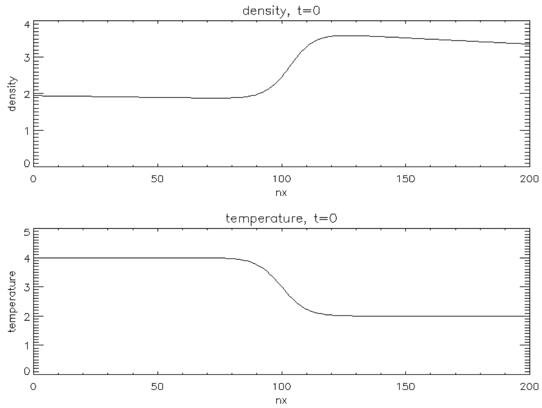

Figure 3.2: 1-D cuts of the density and temperature across the simulation box at $t = 0$.

3.2.1 Theoretical Derivation of Growth Rate

In evaluating the instability without an external magnetic field, we start with the equations:

$$\frac{\partial n}{\partial t} + u \cdot \nabla n + n \nabla \cdot u = 0 \tag{3.4}$$

$$mn \frac{\partial u}{\partial t} + mnu \cdot u = -\nabla p - mng \tag{3.5}$$

$$\frac{\partial}{\partial t}(\frac{p}{n^\gamma}) + u \cdot \nabla \frac{p}{n^\gamma} \tag{3.6}$$

We then linearize the equations using assuming small perturbations such that $n = n_0 + \tilde{n}$, $u = u_0 + \tilde{u}$, etc. Assuming that $u_0 = 0$ and throwing away the second-order terms ($\tilde{u}\tilde{n}$, etc.) results in the equations:

$$\frac{\partial \tilde{n}}{\partial t} + \tilde{u_x} \frac{\partial n_0}{\partial x} + n_0 \nabla \cdot \tilde{u} \tag{3.7}$$

$$mn_0 \frac{\partial \tilde{u}}{\partial t} = -\nabla \tilde{p} - m\tilde{n}g \tag{3.8}$$

$$\frac{\partial}{\partial t}(\tilde{p} - \frac{\gamma p_0}{n_0}\tilde{n}) + p_0 \tilde{u_x} S_0' \tag{3.9}$$

where $S_0' = \frac{\partial}{\partial x} \ln \frac{p_0}{n_0^\gamma}$ and the prime indicates $\partial/\partial x$. We wish to generalize (3.8) above, so we evaluate the term $\hat{y} \cdot \nabla \times$ (3.8), resulting in:

$$\frac{\partial}{\partial t}[n_0(\frac{\partial \tilde{u_z}}{\partial x} - \frac{\partial \tilde{u_x}}{\partial z}) + \frac{\partial n_0}{\partial x}\tilde{u_z}] = g\frac{\partial \tilde{n}}{\partial z} \tag{3.10}$$

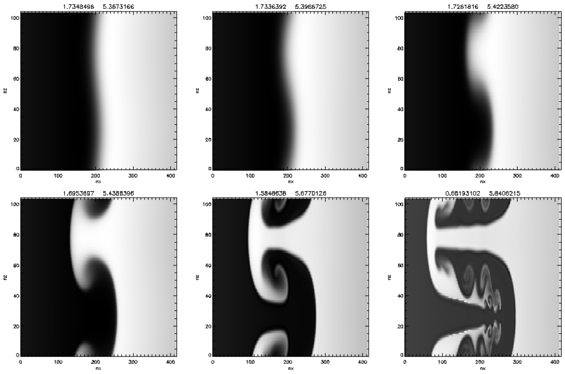

Figure 3.3: The evolution of a Rayleigh-Taylor instability over time. Note the movement of the higher density (white) into the low-density area (black).

We assume that the Rayleigh-Taylor instability occurs on timescales much longer than those of the sound wave, which then requires $\tilde{p} = 0$. As a result, we can simplify (3.9) to:

$$-\gamma \frac{\partial \tilde{n}}{\partial t} + n_o \tilde{u_x} S_0' = 0 \tag{3.11}$$

Now, since we say the variables have the form $n(x) = n_0(x) + \tilde{n}(x)e^{i(kz-\omega t)}$, etc., we can Fourier decompose along $\hat{z}$. This has the effect of replacing all $\frac{\partial}{\partial z}$ with ik and all $\frac{\partial}{\partial t}$ with $-i\omega$. Doing so results in the equations:

$$-i\omega\tilde{n} + \tilde{u_x}\frac{\partial n_0}{\partial x} + n_0\frac{\partial \tilde{u_x}}{\partial t} + ikn_0\tilde{u_z} = 0 \tag{3.12}$$

$$\omega[(\tilde{u_z}n_0)' - ikn_0\tilde{u_x}] = -kg\tilde{n} \tag{3.13}$$

We can also use the Fourier decomposition of equation 3.11 to solve for $\tilde{n}$:

$$\tilde{n} = \frac{-n_0\tilde{u_x}S_0'}{i\omega\gamma} \tag{3.14}$$

Plugging (3.14) into (3.12) and (3.13) gives us:

$$\frac{n_0\tilde{u_x}S_0'}{\gamma} + (\tilde{u_x}n_0)' = -ikn_0\tilde{u_z} \tag{3.15}$$

$$ik(\tilde{u_z}n_0)' + k^2n_0\tilde{u_x} = \frac{k^2 g}{\gamma\omega^2}n_0\tilde{u_x}S_0' \tag{3.16}$$

Substituting (3.15) into (3.16) yields the final eigenvalue equation:

$$[\frac{n_0\tilde{u_x}S_0'}{\gamma} - (\tilde{u_x}n_0)']' + k^2 n_0\tilde{u_x} = \frac{k^2 g}{\gamma\omega^2} n_0\tilde{u_x}S_0' \tag{3.17}$$

Now, we wish to find the functional form for $\tilde{u_x}$. In considering our model, we note that far away from the interface, $S_0' \approx 0$ and $n_0' \approx 0$. Using these approximations in (3.17) and simplifying results in:

$$\tilde{u_x}'' = k^2\tilde{u_x} \tag{3.18}$$

This implies that $\tilde{u_x} \propto Ce^{\pm kx}$. Now, since we have an equation for $\tilde{u_x}$, we can implement this perturbation in the simulation code. However, there also exist perturbations of the density ($\tilde{n}$), temperature ($\tilde{T}$) and the flow velocity in $\hat{z}$ ($\tilde{u_z}$). The density perturbation is given by (3.14). To solve for the temperature perturbation, we remember the assumption used in (3.11) that there are no sound waves, namely that $\tilde{p} = 0$. Since $p = nT$, $\tilde{p} = \tilde{n}T_0 + n_0\tilde{T}$ after throwing away second order terms. In order for $\tilde{p}$ to be equal to zero, we have:

$$\tilde{T} = \frac{-\tilde{n}T_0}{n_0} \tag{3.19}$$

To find $\tilde{u_z}$, we also use the assumption that there are no sound waves. As a result, there is no compression of the flow velocity, so $\nabla \cdot \vec{u} = 0$. Fourier decomposition of this equation and solving for $\tilde{u_z}$ results in:

$$\tilde{u_z} = \frac{-\tilde{u_x}'}{ik} \tag{3.20}$$

We also know that $\tilde{u_x}$ has to be continuous at the interface. So, we can integrate (3.17) across the interface, that is, evaluate $\int_{-\epsilon}^{+\epsilon}(3.17)dx$, where ϵ is infinitesimally small. Because the integral is over a very, very tiny length, all of the finite integrands will each result in adding zero to the final answer. Before we evaluate the integral, we can use an approximation for $S_0' = \frac{\partial}{\partial x}\ln\frac{p_0}{n_0^\gamma}$. Evaluating the derivative and simplifying yields:

$$S_0' = \frac{p'}{p} - \frac{\gamma n'}{n} \tag{3.21}$$

If $p'/p << n'/n$, then we can use the approximation $S_0' \approx \gamma n_0'/n_0$. Using this approximation in the integral and evaluating results in:

$$[-n_0\tilde{u_x'}]_-^+ = \frac{-k^2 g}{\omega^2}\tilde{u_x}[n_0]_-^+ \tag{3.22}$$

In order to evaluate this equation, we remember that $\tilde{u_x}$ is proportional to e^{-kx} when $x > 0$ and e^{+kx} when $x < 0$. Additionally, each side of the interface has a different density. Let n_2 designate the density in the region $x > 0$ which lies on top of the lower density, n_1. Thus, (3.22) can be written as:

$$-n_2(-k)\tilde{u_x} - (-n_1)k\tilde{u_x} = -\frac{k^2 g}{\omega^2}\tilde{u_x}(n_2 - n_1) \tag{3.23}$$

Solving this equation for ω results in:

$$\omega = \pm i\sqrt{kg\frac{n_2 - n_1}{n_2 + n_1}} \tag{3.24}$$

Since ω is imaginary, we define the imaginary part of ω as:

$$\gamma = \sqrt{kg\frac{n_2 - n_1}{n_2 + n_1}} \tag{3.25}$$

Since the time evolution of the instability is represented by $e^{-i\omega t}$, the negative value of ω results in a decay factor $e^{-\gamma t}$ while the positive value of ω results in a growth factor $e^{\gamma t}$. Thus, γ is the growth rate of the Rayleigh-Taylor instability.

Now, we must verify our assumption that the Rayleigh-Taylor instability occurs on timescales much longer than those of the sound wave. We thus define τ_{RT} as the timescale for the instability and τ_s as the sound wave timescale. Since τ_{RT} represents the length of time it takes for the instability to grow, we can say that $\tau_{RT} \propto 1/\gamma$. The time it takes for the sound speed to propagate across the instability is $\tau_s = L/C_s$, where L is the length of the instability and C_s is the sound speed. However, the length is proportional to the wave number, so $L \propto 1/k$, giving us $\tau_s \propto 1/kC_s$. As a result, the ratio of timescales is:

$$\frac{\tau_s}{\tau_{RT}} = \frac{\gamma}{kC_s} = \frac{\sqrt{kg\frac{n_2-n_1}{n_2+n_1}}}{kC_s} \tag{3.26}$$

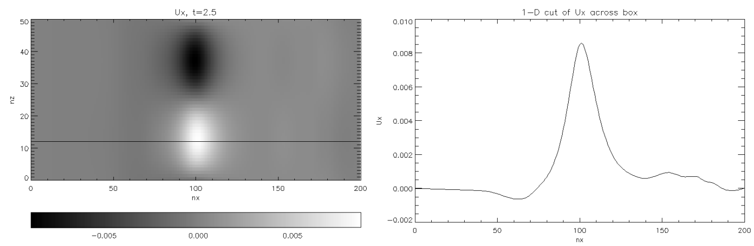

Figure 3.4: A 2-D plot of u_x at $t = 2.5$ and a 1-D cut of u_x across simulation box. The cut of u_x was taken across the black line in the 2-D plot. The maximum value of the plot was used to help find the growth rate.

Squaring both sides and cancelling out like terms yields:

$$(\frac{\tau_s}{\tau_{RT}})^2 = \frac{g\frac{n_2-n_1}{n_2+n_1}}{kC_s^2} \tag{3.27}$$

Now, since $(n_2 - n_1)/(n_2 + n_1)$ is always less than 1 and $C_s \approx 1$, the upper limit on the ratio of timescales can be expressed as $\sqrt{g/k}$. In our simulations, $g = 0.1$ and $k = 2\pi$, giving us a ratio $\tau_s/\tau_{RT} \approx .126 < 1$. Because this is an upper limit, we can conclude that the timescale for the Rayleigh-Taylor instability does occur on timescales much longer than those of the sound wave. Thus, our assumption that $\tilde{p} \approx 0$ is correct.

3.2.2 Computational Growth Rate in Simulation

The full equation for u_x is:

$$\begin{aligned} u_x &= u_0 e^{+kx} e^{ikz} e^{-i\omega t} \ , \ x < x_0 \\ &= u_0 e^{-kx} e^{ikz} e^{-i\omega t} \ , \ x > x_0 \ , \end{aligned} \tag{3.28}$$

where x_0 is half the length of the simulation box. When we plug (3.25) into (3.28), we get the equation:

$$u_x(t) = \tilde{u_0} e^{\sqrt{kg\frac{n_2-n_1}{n_2+n_1}}\ t} \tag{3.29}$$

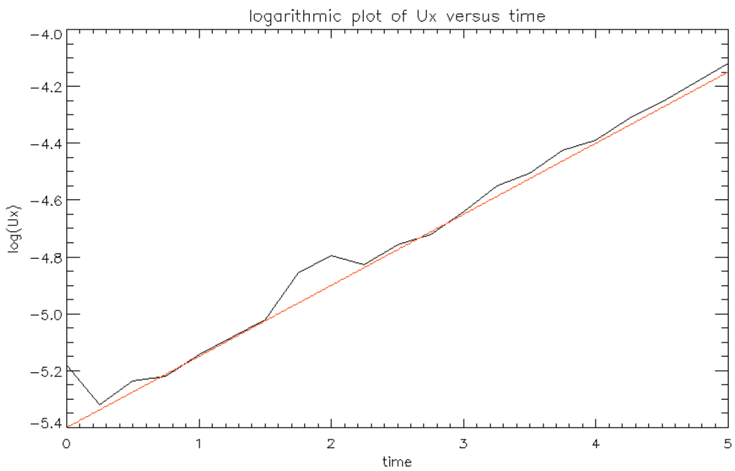

Figure 3.5: A logarithmic plot of the maximum values of u_x at each time interval, the slope of which is the computational growth rate.

where $\tilde{u_0} = u_0 e^{\pm kx} e^{ikz}$. In order to approximate the growth rate from the simulations, we can take the natural log of $u_x(t)$ to get the equation

$$\ln(u_x) = \ln(\tilde{u_0}) + \sqrt{kg\frac{n_2 - n_1}{n_2 + n_1}}\; t \tag{3.30}$$

Note that (3.30) is linear with respect to t. This means that we can take a cut across the simulation box and get the maximum value of u_x at each time interval. Plotting the natural log of these u_x values versus time will result in a graph with a linear slope. Figures 3.4 and 3.5 illustrate our methodology for finding the computational growth rate. The value of this slope should be equal to $\sqrt{kg\frac{n_2-n_1}{n_2+n_1}}$, i.e. the growth rate. However, our implementation of the Rayleigh-Taylor instability in the simulation code (Figure 3.1) does not exactly match some theoretical assumptions we made during the derivation of the growth rate. In theory, we assume that the density and temperature in both regions is constant and that there is a discontinuous jump across the interface between the regions. In order for the code to run smoothly, we had to implement a pressure equilibrium using hyperbolic tangent functions and not a sharp interface between the two regions. Additionally, the density required for an initial equilibrium (eq. 3.3) is not constant in both regions like we assumed. Finally,

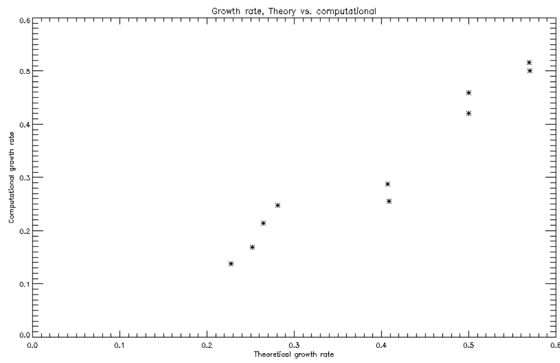

Figure 3.6: Theoretical versus the computational growth rate for $B = 0$.

the theoretical form of u_x (eq. 3.28) has a discontinuous derivative at the interface. In the code, we smoothed over this sharp point so that the simulation could run smoothly. As a result of these differences, we do not expect the calculated theoretical growth rates to exactly match the computational growth rates. We do expect to see a roughly linear relationship between the theoretical and observed growth rates. Any change in the density that causes a change in the theoretical growth rate (eq. 3.25) should also cause a similar, proportional change in the computational growth rate.

The computational growth rates and the values we used to calculate the theoretical growth rates are listed in Table 3.1. Figure 3.6 shows the plot of expected growth rate versus simulated growth rates for various values of n_1, n_2, T_1, and T_2. We see that there is a reasonable agreement between theory and computation.

3.3 Rayleigh-Taylor Instability in Presence of Horizontal Magnetic Field

3.3.1 Theoretical Derivation of Growth Rate

Now, we wish to evaluate the instablilty in the presence of a external magnetic field in the $\hat{z}$ direction. Like above, we start with equations 3.4 and 3.6. However, we also need to add terms for the magnetic field pressure and tension to (3.5) as

Table 3.1: A list of initial values for the temperatures and densities used to calculate the growth rate in the case $B = 0$. In the simulation, $k = 2\pi$ and $g = 0.1$.

T_1	T_2	n_1	n_2	γ_{theory}	γ_{comp}
3	1	1.85	4.3	0.5003	0.4204
3	1	2.5	5.8	0.4998	0.4595
3	2	2.6	3.35	0.2814	0.2476
3	2	2	2.5	0.2642	0.2145
4	2	1.95	3.35	0.4074	0.288
4	2	1.45	2.5	0.4087	0.256
4	3	2	2.45	0.252	0.169
4	3	1.5	1.77	0.2278	0.1385

well as add an equation for the evolution of the magnetic field:

$$mn\frac{\partial u}{\partial t} + mnu \cdot u = -\nabla p - mng - \frac{\nabla B^2}{8\pi} + \frac{B \cdot \nabla B}{4\pi} \tag{3.31}$$

$$\frac{\partial B}{\partial t} = \nabla \times (u \times B) \tag{3.32}$$

As before, we linearize these equations using $n = n_0 + \tilde{n}$, etc., assume $u_0 = 0$, and throw away second order terms. This will result in equations 3.7, 3.9, and:

$$mn_0\frac{\partial \tilde{u}}{\partial t} = -\nabla \tilde{p} - m\tilde{n}g\hat{x} + \frac{B_{0z}}{4\pi m}\frac{\partial}{\partial z}(\tilde{B}_x + \tilde{B}_z) \tag{3.33}$$

$$\frac{\partial \tilde{B}_x}{\partial t} = B_{0z}\frac{\partial \tilde{u_x}}{\partial z} \tag{3.34}$$

$$\frac{\partial \tilde{B}_z}{\partial t} = B_{0z}\frac{\partial \tilde{u_z}}{\partial z} \tag{3.35}$$

Generalizing (3.33) results in:

$$\frac{\partial}{\partial t}[n_0(\frac{\partial \tilde{u_z}}{\partial x} - \frac{\partial \tilde{u_x}}{\partial z}) - \frac{\partial n_0}{\partial x}\tilde{u_z}] = g\frac{\partial \tilde{n}}{\partial z} - \frac{B_{0z}}{4\pi}[\frac{\partial^2}{\partial z^2}\tilde{B}_x - \frac{\partial^2}{\partial z \partial x}\tilde{B}_z] \tag{3.36}$$

As before, we assume no sound wave behavior, so we can simplify (3.9) to (3.11). Now, we decompose the equations along $\hat{z}$. (3.12) will be the same, but (3.34), (3.35), and (3.36) will simplify to:

$$\omega[(\tilde{u_z}n_0)' - ikn_0\tilde{u_x}] = -kg\tilde{n} + \frac{B_{0z}}{4\pi m}(ik^2\tilde{B}_x - k\tilde{B}_z{}') \tag{3.37}$$

$$\tilde{B_x} = \frac{-B_{0z}k}{\omega}\tilde{u_x} \tag{3.38}$$

$$\tilde{B_z} = \frac{-B_{0z}k}{\omega}\tilde{u_z} \tag{3.39}$$

We then plug in the equation for $\tilde{n}$, (3.14), into (3.37) to get:

$$ik(\tilde{u_z}n_0)' + k^2 n_0\tilde{u_x} = \frac{k^2 g}{\gamma\omega^2}n_0\tilde{u_x}S_0' - \frac{B_{0z}}{4\pi m\omega}(k^3\tilde{B_x} + ik^2\tilde{B_z}') \tag{3.40}$$

Now, we plug in equations 3.15, 3.38, and 3.39 into (3.40), yielding:

$$[\frac{n_0\tilde{u_x}S_0'}{\gamma} - (\tilde{u_x}n_0)']' + k^2 n_0\tilde{u_x} = \frac{k^2 g}{\gamma\omega^2}n_0\tilde{u_x}S_0' + \frac{B_{0z}^2k^2}{4\pi m\omega^2}(k^2\tilde{u_x} + ik\tilde{u_z}') \tag{3.41}$$

In order to get rid of $\tilde{u_z}'$, we have to rewrite (3.15) in terms of $\tilde{u_z}'$:

$$[\frac{\tilde{u_x}S_0'}{\gamma} + \frac{(\tilde{u_x}n_0)'}{n_0}]' = -ik\tilde{u_z}' \tag{3.42}$$

Plugging in (3.42) into (3.41) gives us the final eigenvalue equation:

$$[\frac{n_0\tilde{u_x}S_0'}{\gamma} - (\tilde{u_x}n_0)']' + k^2 n_0\tilde{u_x} = \frac{k^2 g}{\gamma\omega^2}n_0\tilde{u_x}S_0' + \frac{B_{0z}^2k^2}{4\pi m\omega^2}(k^2\tilde{u_x} + [-\frac{\tilde{u_x}S_0'}{\gamma} - \frac{(\tilde{u_x}n_0)'}{n_0}]') \tag{3.43}$$

As before, we wish to find the functional form of $\tilde{u_x}$. Using the approximations $S_0' \approx 0$ and $n_0' \approx 0$, we get:

$$\tilde{u_x}'' - k^2\tilde{u_x} = \frac{-B_{0z}^2k^2}{4\pi m n_0\omega^2}(k^2\tilde{u_x} - \tilde{u_x}'') \tag{3.44}$$

Note that the square of the Alfvén speed is $C_A^2 = \frac{B_{0z}^2}{4\pi m n_0}$, so we can simplify eq. 3.44 to:

$$\tilde{u_x}''(1 - \frac{C_A^2k^2}{\omega^2}) = \tilde{u_x}k^2(1 - \frac{C_A^2k^2}{\omega^2}) \tag{3.45}$$

Canceling out like terms results in eq. 3.18 which was obtained from evaluating the instability with no external magnetic field. As a result, $\tilde{u_x}$ has the same form as above, i.e. $\tilde{u_x} = u_0e^{\pm kx}e^{ikz}e^{-i\omega t}$. Like before, there exist perturbations in the density, the temperature, and u_z, given by equations 3.14, 3.19, and 3.20, respectively. However, due to the addition of the magnetic field, there are also perturbations in

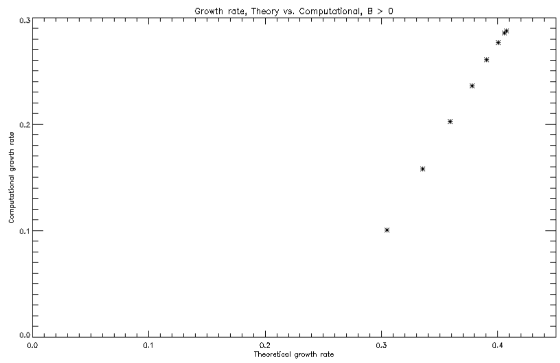

Figure 3.7: Theoretical versus the observed growth rate for $T_1 = 4$, $T_2 = 2$, $n_1 = 1.95$, $n_2 = 3.35$ and various values of B_0 from 0.01 to 0.07.

B_x and B_z. These perturbations are given by (3.38) and (3.39), respectively. However, since the magnetic field is governed by ψ, we must introduce a perturbation in ψ that will result in the required $\tilde{B_x}$ and $\tilde{B_z}$:

$$\tilde{\psi} = \frac{-B_0 z}{\omega}\tilde{u_x} \tag{3.46}$$

Now, since $\tilde{u_x}$ has to be continuous at the interface, we can integrate the eigenvalue equation (3.43) across the interface. So, like above, we will evaluate $\int_{-\epsilon}^{+\epsilon}(3.43)dx$, with ϵ being infinitesimally small. Remembering that the finite integrands will not contribute anything to the integral and that $S_0' \approx \gamma n_0'/n_0$, the integral evaluates to:

$$[-n_0\tilde{u_x'}]_-^+ = \frac{-k^2 g}{\omega^2}\tilde{u_x}[n_0]_-^+ + \frac{B_{0z}^2 k^2}{4\pi m\omega^2}[-\tilde{u_x}']_-^+ \tag{3.47}$$

As before, we remember that $\tilde{u_x} \propto e^{-kx}$ for $x > 0$ and e^{kx} for $x < 0$. Additionally, n_2 is the density for the region $x > 0$ and n_1 is the density for the region $x < 0$. After evaluating (3.47), the result is:

$$n_2 k\tilde{u_x} + n_1 k\tilde{u_x} = -\frac{k^2 g}{\omega^2}\tilde{u_x}(n_2 - n_1) + \frac{B_{0z}^2 k^2}{4\pi m\omega^2}(2k\tilde{u_x}) \tag{3.48}$$

Solving for ω results in:

$$\omega = \pm i\sqrt{kg\frac{n_2 - n_1}{n_2 + n_1} - \frac{B_{0z}^2 k^2}{2\pi m(n_2 + n_1)}} \tag{3.49}$$

Table 3.2: A list of initial values for the magnetic field strength used to calculate the growth rate in the case $B > 0$. In the simulation, $n_1 = 1.95$, $n_2 = 3.35$, $T_1 = 4$, $T_2 = 2$, $k = 2\pi$ and $g = 0.1$.

B_0	γ_{theory}	γ_{comp}
0.01	0.4056	0.2859
0.02	0.40015	0.2765
0.03	0.3906	0.2603
0.04	0.377	0.2364
0.05	0.3588	0.2025
0.06	0.3352	0.1583
0.07	0.3049	0.1009

Notice that this equation has not been normalized. Normalizing (3.49) results in:

$$\omega = \pm i\sqrt{kg\frac{n_2 - n_1}{n_2 + n_1} - \frac{2B_{0z}^2 k^2}{(n_2 + n_1)}} \tag{3.50}$$

Similar to above, we define γ as the imaginary part of ω. This results in the growth rate:

$$\gamma = \sqrt{kg\frac{n_2 - n_1}{n_2 + n_1} - \frac{2B_{0z}^2 k^2}{(n_2 + n_1)}} \tag{3.51}$$

An interesting result of (3.50) is that for B_0 sufficiently large, the term in the radical becomes negative, and we can factor out a imaginary number. As a result, both the imaginary numbers cancel out and ω becomes real. The time evolution of the instability can thus be expressed by $e^{i\gamma t}$, indicating an oscillation of the instability. The physical meaning of this is that if the magnetic field is too strong, it will confine the Rayleigh-Taylor instability. The result of this confinement is the oscillation of the magnetic field lines, an Alfvén wave.

3.3.2 Computational Growth Rate in Simulation

In order to measure the growth rate in the simulation, we can use $u_x(t) = \tilde{u_0} e^{\sqrt{kg\frac{n_2-n_1}{n_2+n_1} - \frac{2B_{0z}^2 k^2}{(n_2+n_1)}}}$. Taking the natural log of $u_x(t)$ results in the linear equation:

$$\ln(u_x) = \ln(\tilde{u_0}) + \sqrt{kg\frac{n_2 - n_1}{n_2 + n_1} - \frac{2B_{0z}^2 k^2}{(n_2 + n_1)}}\ t \tag{3.52}$$

We use the same method as above to calculate the computational growth rate (Figures 3.4 and 3.5). Table 3.2 lists the values used to calculate the theoretical growth rate. Much like above, our implementation of the Rayleigh-Taylor instability in the simulation code does not exactly match some theoretical assumptions we made during the derivation of the growth rate. As a result, our calculated theoretical values for the growth rate do not exactly match our computational values for the growth rate, though we still expect to see a rough linear relationship between theory and observation. Figure 3.7 shows the plot of expected growth rate versus simulated growth rates for values of B_0 from 0.01 to 0.08 with $T_1 = 4$, $T_2 = 2$, $n_1 = 1.95$, and $n_2 = 3.35$. There is a clear linear relationship between theory and observation, which is what we expect to see.

Chapter 4

THE CENTRIFUGAL BREAKOUT MODEL

4.1 Modifying the Code

Since the code has passed all of its benchmarks, we can now modify it to simulate centrifugal breakout. Two major changes to the code are needed: a source that gradually adds density to the simulation box over time and the introduction of a centrifugal force acting upon the plasma. In order to add a source for the density, we simply add a source term, δn, to the density equation (2.4):

$$\frac{\partial n}{\partial t} = -\frac{\partial J_{px}}{\partial x} - \frac{\partial J_{pz}}{\partial z} + \delta n \tag{4.1}$$

Since we wish to add density in a particular location within the box, i.e. the center, and not anywhere else, we give δn the functional form:

$$\delta n = s_0 e^{-(x-x_0)^2/w_0} e^{-(z-z_0)^2/w_0}, \tag{4.2}$$

where s_0 controls the amount of density the source is pouring into the simulation and w_0 determines the width of the source. This has the effect of adding density to a circular location in the center of the simulation box. Figure 4.1 shows a picture of the difference between the density after one hundred time steps and the initial density. The source can clearly be seen in the center of the box. One side effect of this density source is the unintentional addition of a pressure source. The addition of δn results in a change to the pressure equation:

$$p_i + \delta p = (n_i + \delta n)T, \tag{4.3}$$

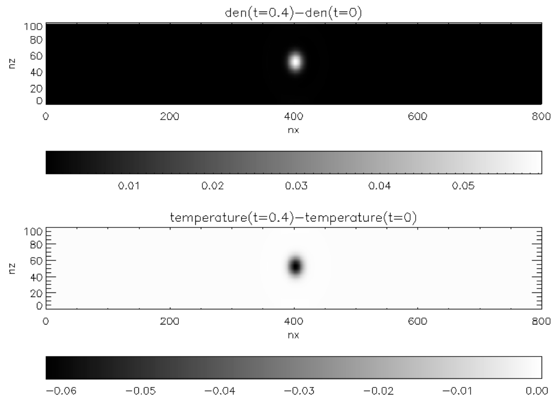

Figure 4.1: This figure shows the difference between the density after 100 time steps ($t = 0.4$) and the initial density ($t = 0$), as well as the the difference between the temperature after 100 time steps ($t = 0.4$) and the initial temperature ($t = 0$). Note that δT is the opposite of δn, which is to be expected since there is no pressure source/sink (i.e. $\delta p = 0$.

where the subscript i indicates the time step. Since $p = nT$, (4.3) simplifies to $\delta p = \delta n/T$. We do not want the addition of a pressure source, i.e. δp has to equal zero. If we set $\delta p = 0$ and introduce a temperature source such that $T = T_i + \delta T$ in (4.3), solving for δT results in the equation:

$$\delta T = \frac{-\delta n T_i}{n_i + \delta n} \tag{4.4}$$

In order to implement this within the code, we took the adiabatic term from (2.10) and added a source $\delta(p/n^\gamma)$:

$$\frac{p}{n^\gamma} + \delta(\frac{p}{n^\gamma}) = \frac{p_i + \delta p}{(n_i + \delta n)^\gamma} \tag{4.5}$$

Using $\delta p = 0$ and solving for $\delta(p/n^\gamma)$ results in:

$$\delta(\frac{p}{n^\gamma}) = \frac{p_i}{(n_i + \delta n)^\gamma} - \frac{p}{n^\gamma} \tag{4.6}$$

Adding this source to (2.10) results in a temperature sink that effectively nullifies the increase in pressure caused by the density source. This sink is seen in Figure

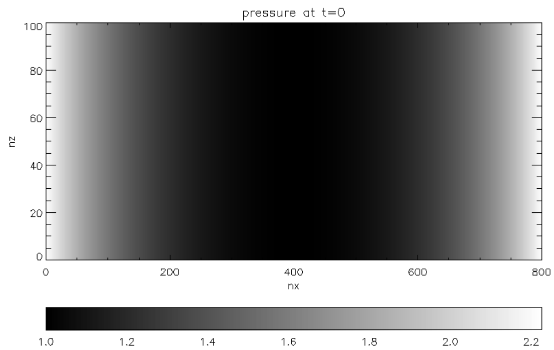

Figure 4.2: This figure shows the initial pressure of the implemented equilibrium for centrifugal breakout.

4.1. Another necessary addition to the code is the modification of the gravitational force found in eq. 2.9 into a combined gravitational-centrifugal force. To do so, we remember that the rigidly rotating magnetosphere discussed in Section 1.3.3 around the star results in a centrifugal force $F_c = m\Omega^2 r$. As a result, the total gravitational-centrifugal acceleration can be represented by:

$$a = g_1 \frac{x - x_0}{L_x}, \tag{4.7}$$

where g_1 represents the strength of the combined forces, L_x represents the length of the box, and x_0 represents the Keplerian radius (eq. 1.16) so that at $x = x_0$, the centrifugal force cancels out the gravitational force. Substituting this for the normal gravitational acceleration g in 2.9 results in:

$$\frac{\partial J_{px}}{\partial t} = -\frac{\partial}{\partial x}(u_x J_{px}) - \frac{\partial}{\partial z}(u_z J_{px}) - \frac{\partial \psi}{\partial x}\left(\frac{\partial^2 \psi}{\partial x^2} + \frac{\partial^2 \psi}{\partial z^2}\right) - \frac{\partial}{\partial x}\frac{B_y^2}{2} - \frac{\partial}{\partial x}(nT) - n g_1 \frac{x - x_0}{L_x} \tag{4.8}$$

4.2 The Model

Since we changed eqs. 2.4, 2.10, and 2.9 to eqs. 4.1, 4.5, and 4.8, we need to change our equilibrium from (3.1) to:

$$\nabla p = \nabla(nT) = -m n g_1 \frac{(x - x_0)}{L_x}\hat{x} \tag{4.9}$$

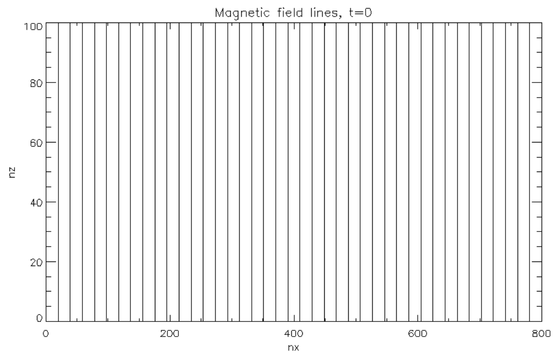

Figure 4.3: This figure shows the initial magnetic field lines at $t = 0$ for $B_z = 0.01$

However, unlike the Rayleigh-Taylor equilibrium, we take the temperature to be constant. We do this since the plasma in the rigidly rotating magnetosphere is roughly at the same temperature throughout. With T as constant, we can solve for the density:

$$n = e^{\frac{g_1}{T}\frac{x-x_0}{L_x}} \tag{4.10}$$

Figure 4.2 shows the initial pressure in this equilibrium. This figure is expected given the force term (4.7), since the density has a tendency to flow from a high pressure to a low pressure region. This difference in pressure is countered by the gravitational-centrifugal force. In order to approximate the magnetic field loops of the star, we first consider the size of the loops. For a star with moderate magnetic confinement, $\eta_* \approx 500 - 600$, and for a star with large magnetic confinement, like σ Ori E, $\eta_* \approx 10^7$ [2]. Using (1.14), we get a value for the Alfvén radius between 5 and 56 times the stellar radius. Since R_A, the maximum radius for a magnetic field loop from the star, is so large, we can say that the magnetic field at the top of the field loop is approximately perpendicular to the gravitational-centrifugal force. Because of this, our simulation incorporates a magnetic field perpendicular to the force, i.e. in the $\hat{z}$ direction, as seen in Figure 4.3.

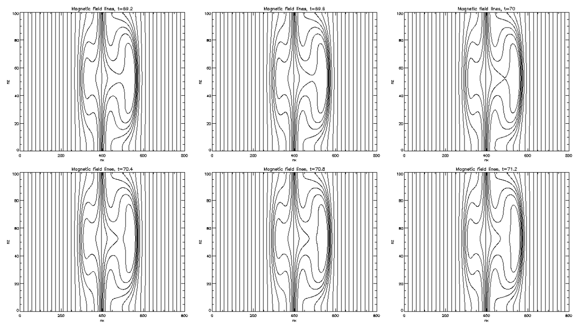

Figure 4.4: This figure shows the progression of reconnection between $t = 69.2$ and $t = 71.2$. Note the configuration of the magnetic field lines in an X in the upper right hand figure, at $t = 70$. This is a result of reconnection. The initial magnetic field was $B_z = 0.01$.

4.3 Simulations of Magnetic Reconnection from Centrifugal Breakout

After setting the initial conditions, the simulation is run for many, many time steps. Eventually, the buildup of mass in the center of the box causes a large increase in the gravitational-centrifugal force, pushing the mass out towards the edges of the box. The mass drags the field lines along with it, forcing reconnection. Figure 4.4 shows the progression of the magnetic field lines toward reconnection. Remembering that in simple reconnection (Figure 1.1), the plasma flows towards the X-line from the top and bottom and away from the X-line on the left and the right, we can see in Fig. 4.4 the movement of the magnetic field lines towards the X-line prior to reconnection and then moving away from the X-line afterwards. This confirms that there is reconnection occurring in the simulation, though it is of a more complex form than depicted in Fig. 1.1. Note that due to the nature of the combined gravitational-centrifugal force implemented in the simulation, there are actually two regions in which the magnetic field is being stretched, one to the left of x_0, and one to the right. Interestingly, the onset of reconnection occurs much faster in the region $x > x_0$ than for $x < x_0$.

Another point of interest for these centrifugal breakout simulations is the characteristic breakout time, $t_b \propto \eta_*$ (eq. 1.20). For higher levels of magnetic

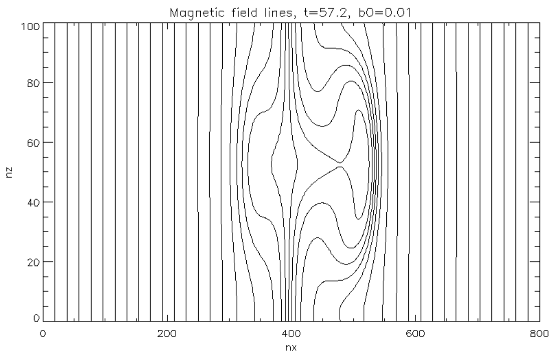

Figure 4.5: This figure shows the magnetic field lines at $t = 57.2$ and $b_0 = 0.01$. Note that the magnetic field lines are undergoing reconnection as evidenced by the X-line present in the figure.

confinement, the breakout time should be longer. This was tested by running simulations for different values of b_0 and comparing the magnetic field lines at a particular time, $t = 57.2$. This time was chosen since this was the first occurrence of reconnection for the $b_0 = 0.01$ case. Figures 4.5, 4.6, and 4.7 show the magnetic field lines for $b_0 = 0.01$, $b_0 = 0.02$, and $b_0 = 0.05$, respectively. From these pictures, we see that the $b_0 = 0.01$ case is undergoing reconnection while the $b_0 = 0.02$ case will experience reconnection in the near future. For $b_0 = 0.05$, the magnetic confinement is so strong that the density source has barely made a dent in the field lines. We can thus conclude that there is a positive correlation between b_0 and the characteristic breakout time.

4.4 Future Work

The work presented in this chapter is a very solid base with which to investigate reconnection occurring as a result of centrifugal breakout. However, there are still some issues. One issue is a problem with the boundary conditions. Ideally, the boundary condition for J_{px} would be extrapolating, meaning that if the mass was on its way out of the simulation box, it would continue to flow out of the box. Likewise, if the mass on the edge of the box was flowing towards the center, then mass on the

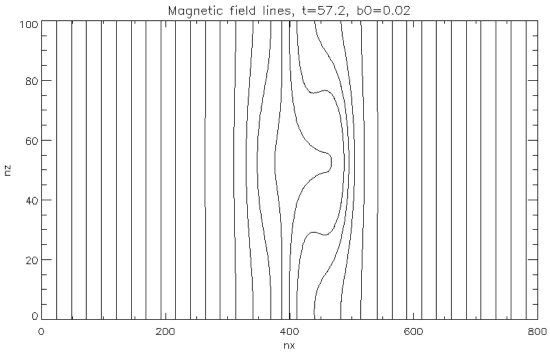

Figure 4.6: This figure shows the magnetic field lines at $t = 57.2$ and $b_0 = 0.02$. Note that the magnetic field lines have not yet undergone reconnection as in the $b_0 = 0.01$ case.

"outside" would flow into the box. However, there is some issue with the boundary conditions, which has the effect of causing the entire contents of the box to float off to the right and out of the simulation. This effect is seen in Figure 4.8. In order to remedy this problem, we set the boundary conditions for J_{px} to be asymmetric and made the box longer. Since the box is longer, the field lines undergoing reconnection are not pressed up against the sides of the simulation. In comparing Figures 4.5 and 4.3, we see that there is no change in the magnetic field near the edges of the simulation box, so the reconnection occurring within the simulation is unaffected by the boundary conditions. However, for future simulations, it would be ideal to have an extrapolating boundary condition for J_{px} so that the box could be made smaller and the time needed to run the code would be cut in half. Another issue for future work is the nature of the magnetic field used in the simulation. Currently, the magnetic field lines are initialized perpendicular to the centrifugal force. However, in ud-Doula and Owocki's 2006 centrifugal breakout paper [2], the magnetic field used was a dipole, as seen in Figure 1.3. The different configuration of magnetic field lines could have an effect on the rate of centrifugally-induced reconnection. The straight field lines employed in our simulation may require more plasma for the centrifugal force to bend and stretch them out. The curvature of the field lines in the

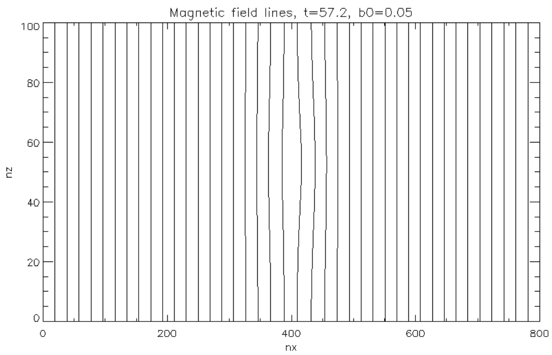

Figure 4.7: This figure shows the magnetic field lines at $t = 57.2$ and $b_0 = 0.05$. Note that the magnetic field lines have not yet undergone reconnection like in the $b_0 = 0.01$ case, nor have bent as much as in the $b_0 = 0.02$ case.

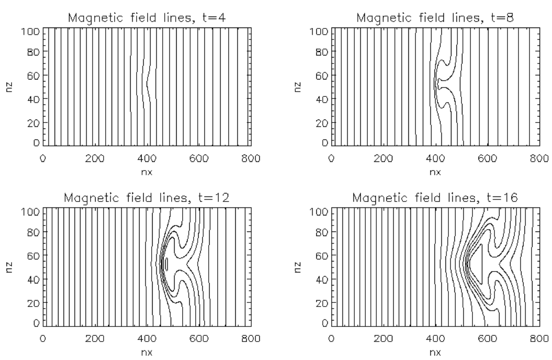

Figure 4.8: This figure shows the gradual drifting of the simulation out of the box. Note that if no drifting were present, the reconnection would be occurring near $nx = 300$.

dipole field may make it easier for the plasma to stretch out the magnetic field and cause reconnection. Further study is needed to determine if there is any difference in the characteristic breakout time between a straight magnetic field and a dipole magnetic field. Additionally, with a dipole field, a breakout ultimately leads to a blob of reconnected plasma and magnetic field escaping from the star's magnetic field. However, in our simulations, the 1D nature of our equilibrium leads to compression of the magnetic field lines, stopping the breakout. In a future study, we plan to implement a dipole-like curved field line equilibrium in which magnetic field line tension is balanced out by centrifugal force. We hope that such an equilibrium would lead to a stronger breakout of material.

REFERENCES

[1] R.A. Scheper and A.B. Hassam. Line-tying and the reduced equations of magnetohydrodynamics. *The Astrophysical Journal*, 511: 976-980, February 1999.

[2] A. ud-Doula, R.H.D. Townsend, and S.P. Owocki. Centrifugal breakout of magnetically confined line-driven stellar winds. *The Astrophysical Journal*, 640: L191-194, April 2006.

[3] R.H.D. Townsend and S.P. Owocki. A rigidly rotating magnetosphere model for circumstellar emission from magnetic OB stars. *Monthly Notes of the Royal Astronomical Society*, 357:251-264, 2005.

[4] A. ud-Doula and S.P. Owocki. Dynamical simulations of magnetically channeled line-driven stellar winds in isothermal, nonrotating, radially driven flow. *The Astrophysical Journal*, 576:413-428, September 2002.

[5] J. Sanz-Forcada, E. Franciosini, and R. Pallavicini. XMM-*Newton* observations of the σ Ori cluster. *Astronomy and Astrophysics*, 421:715-727, July 2004.

[6] S. P. Owocki. Stellar Magnetospheres. Personal notes, 2008.

[7] H. Alfvén. On the existence of electromagnetic-hydrodynamic waves. *Ark. Mat., Astron. o. Fys.* 29B: 1-7, 1942.

[8] A. ud-Doula, S.P. Owocki, R.H.D. Townsend. Dynamical simulations of magnetically-channelled line-drived stellar winds - II. The effects of field-aligned rotation. *Monthly Notes of the Royal Astronomical Society*, 385:97-108, 2008.